Available online at www.sciencedirect.com
ScienceDirect
Journal of Nuclear Materials 362 (2007) 104–115
journal of nuclear materials
www.elsevier.com/locate/jnucmat

Characterization of phases in ‘crud’ from boiling-water reactors by transmission electron microscopy

Dawn E. Janney *, Douglas L. Porter

Idaho National Laboratory, Idaho Falls, ID 83415, USA

Received 25 July 2006; accepted 20 November 2006

Abstract

This paper reports phases identified in samples of crud (activated corrosion products) from two commercial boiling-water reactors using transmission and analytical electron microscopy and selected-area electron diffraction. Franklinite ($ZnFe_2O_4$) was observed in both samples. Hematite (α-Fe_2O_3), crystalline silica (SiO_2), a fine-grained mixture of iron oxides probably including magnetite (Fe_3O_4), hematite (α-Fe_2O_3), and goethite (α-FeOOH), and an unidentified high-Ba, high-S phase were observed in one of the samples. Willemite (Zn_2SiO_4), amorphous silica, and an unidentified iron–chromium phase were observed in the other. Chloride-bearing phases were found in both samples, and are assumed to represent sample contaminants. Because of the small sample volumes and numbers of particles studied and the possibility of contamination, it is not clear whether the differences between the phases observed in the two crud samples represent actual differences in the assemblages formed in the reactors.

PACS: 61.14.−x; 82.80.Ej; 28.52.Fa; 91.67.Gy

1. Introduction

Activated corrosion products from structural elements in light-water reactors (‘crud’) are of concern to the nuclear power industry for at least two reasons: (1) Particularly in boiling-water reactors (BWRs), a large fraction of these corrosion products deposit on the outer surfaces of fuel rods [1], where they can compromise the thermal efficiency of the fuel rods and perhaps lead to cladding breach and fuel-rod failure. (2) Crud can become detached from the locations in which it forms, causing radioactive contamination in cooling-water systems and spent-fuel storage areas (e.g., [2]). Characterizations of BWR crud from operating reactors are rare in the open literature, but suggest that relatively small changes in plant water chemistry and operating conditions can significantly affect the rate of crud buildup, as well as the thermal properties, phases present, and tenacity (resistance to becoming detached) of the crud.

Several approaches have been used to identify the phases in crud. In one approach (e.g., [3,4]), researchers have simulated formation of crud by

* Corresponding author. Tel.: +1 208 533 7478; fax: +1 208 533 7996.
E-mail address: dawn.janney@inl.gov (D.E. Janney).

0022-3115/$ - see front matter
doi:10.1016/j.jnucmat.2006.11.009

boiling water with a composition similar to that in reactor cooling-water systems and analyzed the resulting phases using X-ray diffraction. A second approach involves modeling of the effects of the radiolysis of water in the reactor on the formation of specific minerals [5]. A third approach involves attempting to infer the phases present from crystal morphologies and proportions of elements in chemical analyses involving large numbers of crystals [6].

Although each of these approaches provides important information, none of them directly identifies the phases present in actual crud. Accurate phase identification is important for at least three reasons: (1) it may provide a more sensitive approach to evaluating the effects of operational changes than can be obtained from bulk chemistry alone; (2) it allows evaluation of the extent to which properties of simulated crud can be used to design strategies for operating reactors; and (3) models of crud formation and remediation processes are likely to require kinetic and thermodynamic data about nucleation, growth, and perhaps dissolution of specific phases. This study uses transmission electron microscopy (TEM) and selected-area electron diffraction (SAED) to identify the phases present in samples of crud from two commercial boiling-water reactors.

2. Samples

As part of a continuing effort to improve the Department of Energy's ability to address problems in currently operating commercial nuclear reactors, the Electric Power Research Institute (EPRI) arranged for the Idaho National Laboratory (INL) to be sent samples of crud from two commercial BWRs for analysis. Both samples were reported to be collected by scraping them from the outsides of fuel pins taken from the reactors during normal refueling operations using razor blades in a hot cell.

Sample A was from a failed two-cycle rod that had a cumulative burnup of 38.3 GWd/MTU. It was collected at the ~230 cm elevation (believed to be below the elevation of the primary failure). Sample B was collected from the ~75 cm elevation on a three-cycle rod that had a cumulative burnup of 40.7 GWd/MTU. Both rods had thick deposits of tenacious crud, and both samples were from plants that used Zn addition and Noble Metal Chemical Addition (NMCA). Independent analyses of samples collected at the same time and from the same locations by commercial laboratories were described in Ref. [6].

3. Methods

Small amounts of each crud sample were prepared for analysis by transmission electron microscopy (TEM) in the Electron Microscopy Laboratory (EML) at the INL. Each TEM sample was prepared by transferring a few crud particles into a clean 30 ml polyethylene bottle with tweezers or a clean paintbrush, adding ~10 ml of purified water, intermittently ultrasonicating the bottle for several days, shaking the bottle, transferring a drop of the liquid from the bottle to a commercially prepared carbon-coated formvar film supported by a 300-mesh gold grid, and air drying. Although the crud particles did not appear to disaggregate and the water remained clear, TEM examination showed numerous fine particles dispersed on the formvar films. The particles did not appear to be electrostatically charging during examination, and thus were not coated with carbon.

After halite (NaCl) was identified in TEM analyses of both samples, ~60 ml of water taken from the wash bottle used for TEM sample preparation were submitted to the Analytical Laboratory at the INL for measurement of chloride concentration. As no water was added to the wash bottle between preparing the TEM samples and collecting the sample for chloride analysis, the chloride analysis can be considered representative of the composition of the water used to prepare the TEM samples. Ion chromatography measurements showed that the water had 0.3–0.4 ppm chloride – somewhat higher than would be expected from ultrapure water, but clearly not enough to be the source of the chlorine in the observed chlorides. Independent SEM analyses of a sample collected at the same time and from the same location as sample B carried out at another laboratory also showed the presence of chloride [6]. It is highly unlikely that significant concentrations of chloride would be tolerated in a reactor cooling system; thus the chloride apparently represents a contaminant introduced between the time the fuel pin was removed from the reactor and the time the samples were sent to the INL and the independent laboratory for analysis.

Data was collected using a JEOL 2010 transmission electron microscope equipped with a double-tilt (±20°, ±30°) analytical holder and a LaB_6 filament. The microscope was operated at a nominal voltage of 200 kV. Images and diffraction patterns were collected digitally with a Gatan Ultrascan camera and Gatan Digital Micrograph software, version 3.10.0 for GMS 1.5.0.

Energy-dispersive (EDX) spectra were collected using an Oxford Link Petafet EDX detector with a SiLi crystal, nominal 20 eV channel width, nominal energy range from 0 to 20 keV, and nominal 136 eV resolution. The spectra were collected and quantified using Link ISIS software, Isis Suite revision 3.2, with peak profiles and *k*-factors supplied by the manufacturer. Each spectrum was quantified individually based on a qualitative analysis including both peaks identified by the software and those identified from visual inspection of the spectrum. Although peaks from C and O were commonly observed, these elements were generally not quantified because it was not possible to determine the appropriate absorption and fluorescence corrections (which are dependent on local sample geometry and composition and are particularly important for low-energy X-rays such as those produced by C and O). Peaks from Au were ignored because it was assumed that they were from the grid. Other elements may be present in low concentrations but were not recognized because of peak overlaps.

Small peaks from Fe and Co are common in EDX spectra collected with the sample holder used in this study, even from samples in which these elements are not present. As Fe and Co are likely constituents of the samples analyzed here, both elements were included in quantification. Reported concentrations of these elements may be slightly over-stated.

Diffraction patterns were typically collected using selected-area apertures with effective diameters of 250 or 600 nm. Images and diffraction patterns with rings were typically collected with the sample tilted 10° towards the EDX detector. Diffraction patterns with individual reflections were collected by tilting the sample through the entire range allowed by the specimen holder and recording patterns from all major zone axes. The earliest data was collected using a nominal camera length of 30 cm, which provided bright patterns with sharp rings but made it difficult to see rings with small radii. A camera length of 50 cm (which provided better information about rings with smaller radii but produced less intense, somewhat less sharp, rings) was used for later data.

Camera constants relating distances measured on diffraction patterns to lattice-plane spacings ('d-spacings') were calibrated using diffraction patterns from nanocrystalline gold. All calibration and experimental data were collected with lens settings as close to identical as possible.

The phases producing each diffraction pattern with rings were identified by measuring the radius of each ring, converting it to a d-spacing, estimating relative intensities of all of the rings in each diffraction pattern, and comparing the resulting d-spacings and relative intensities to the PDF4+ database (International Centre for Diffraction Data) after narrowing the search using qualitative chemical data from EDX spectra. In principle, a perfect match between the PDF4+ database and the experimental diffraction pattern would imply that each of the high-intensity rings in the experimental pattern corresponded to a high-intensity d-spacing in the database and that the database did not show any high-intensity reflections not matched by rings in the experimental data. In practice, it was not possible to match some of the rings in some diffraction patterns, suggesting that these patterns represented mixtures including phases that were not identified.

The phase producing each single-crystal diffraction pattern was identified by compiling a list of possible phases based on the EDX data, converting measured spot spacings and angles to d-spacings and interplanar angles for each possible phase, and attempting to index all reflections in each diffraction pattern by comparison to the d-spacings and interplanar angles in each candidate phase. Phases that could not produce the observed d-spacings and interplanar angles were discarded as possible identifications, and any kinematically forbidden reflections in the experimental patterns were noted for later analysis.

4. Results

Franklinite ($ZnFe_2O_4$), willemite, hematite (α-Fe_2O_3), akaganéite (β-FeOOH), nanocrystalline mixtures containing more than one iron oxide, and crystalline and amorphous silica were identified from diffraction and EDX data in at least one sample each. Diffraction and EDX data from two phases (one high in Ba and S, and one high in Fe and Cr) that could not be identified by comparison to the PDF4+ database were also collected.

Many TEM images of sample B show thin deposits of material surrounding thicker particles. EDX spectra from the thin deposits characteristically show high concentrations of Na and Cl. Rings in the corresponding diffraction patterns correspond to d-spacings from halite (NaCl). Ratios of Na to Cl in some spectra are far greater than 1, suggesting the possibility that the areas contain other Na phases not represented in the diffraction patterns. Similar thin deposits including both halite and sylvite (KCl) were observed in sample A, but were far less common than in sample B.

These thin deposits probably represent water-soluble phases that dissolved while the samples were wet, and were precipitated as halite or sylvite as the water used to prepare the TEM samples dried. Although the identities of the original water-soluble phases are unknown, it is unlikely that the high concentrations of chlorine required to produce them would have been present inside a reactor. Thus, the water-soluble phases are interpreted as contaminants and data from them will not be considered further in this paper.

4.1. Franklinite ($ZnFe_2O_4$)

Fig. 1(a) shows a fine-grained material from sample A whose EDX spectra (Table 1) indicate a Zn:Fe ratio of ~1:2. The eight largest d-spacings represented by rings in the corresponding diffraction

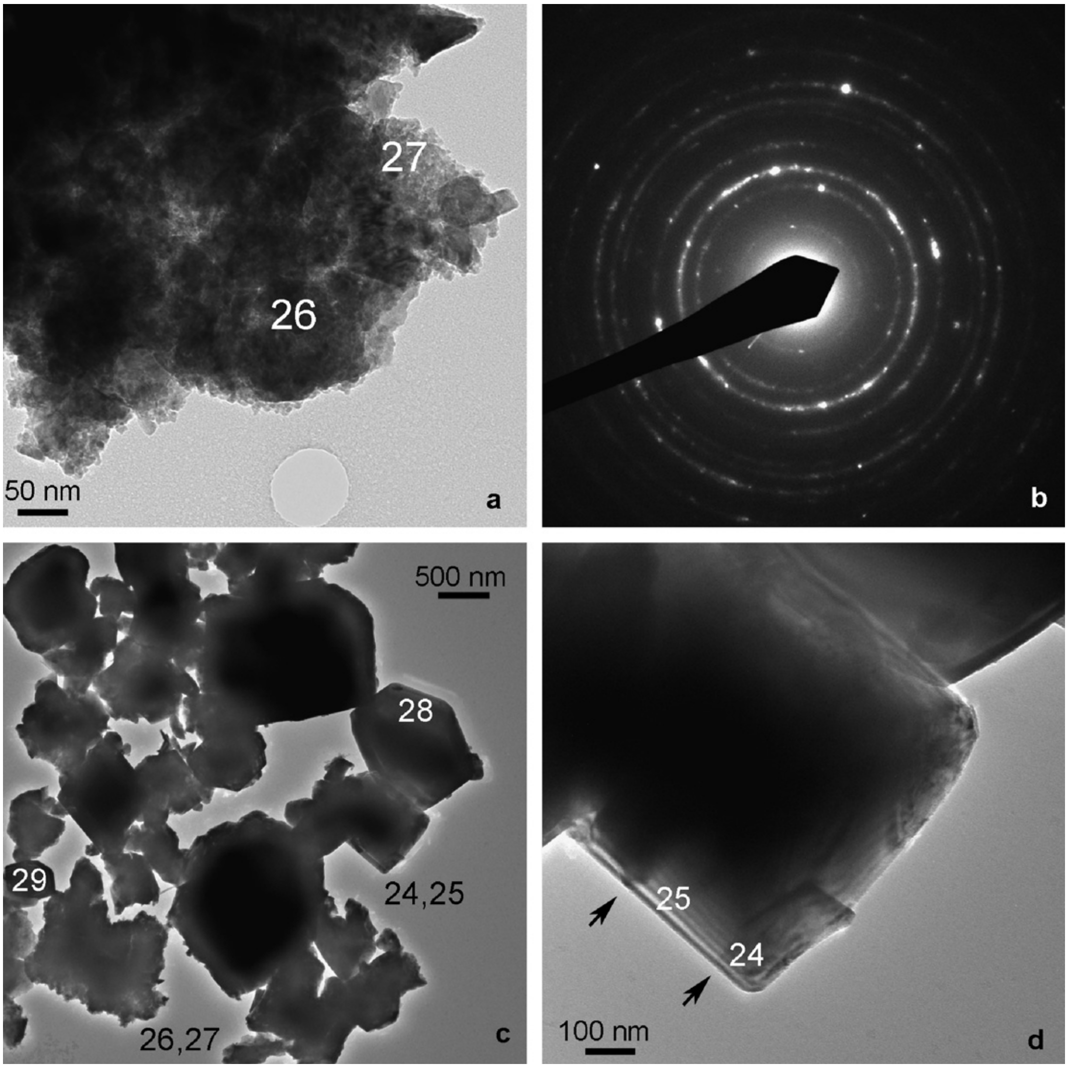

Fig. 1. Franklinite ($ZnFe_2O_4$), sample A. (a) Image of area with spectra A-26 and A-27. (b) Diffraction pattern including the entire area shown in part c. (c) Image showing numerous crystals, some of which were identified as franklinite. Numbers indicate locations of EDX spectra in Tables 1 and 2. (d) Image of crystal with spectra A-24 and A-25. Arrows indicate planar defects in the crystal structure.

Table 1
EDX data from fine-grained franklinite, sample A

Element	Spectrum A-1		Spectrum A-26		Spectrum A-27	
	wt%	at.%	wt%	at.%	wt%	at.%
Na			3.8	8.9	5.1	11.5
Al	0.5	1.0	1.7	3.4	3.1	6.1
Si	0.3	0.6	0.9	1.7	1.2	2.2
P					1.9	3.2
Cl			1.5	2.3	0.9	1.3
K			0.5	0.7	0.6	0.8
Ca			0.7	0.9	1.1	1.4
Cr	16.0	17.7	1.5	1.6	0.4	0.4
Mn	2.2	2.3	3.9	3.8	5.1	4.9
Fe	47.9	49.4	51.8	50.1	46.6	43.7
Ni	4.6	4.5	2.5	2.3	1.3	1.2
Cu					0.6	0.5
Zn	26.0	22.9	27.8	23.0	25.6	20.5
Sr					0.2	0.1
Zr	2.6	1.6			6.4	2.5
Ba			3.3	1.3		

Locations from which spectra A-26 and A-27 were collected are shown by the corresponding numbers in Fig. 1(c). Percentages of reported elements are normalized to a total of 100% for each spectrum.

pattern (Fig. 1(b)) are 0.127, 0.148, 0.162, 0.172, 0.210, 0.251, 0.297, and 0.482 nm. These d-spacings match all of the high-intensity d-spacings greater than 0.125 nm from franklinite in the PDF4+ database (e.g., card 00-022-1012) to within measurement error. Thus, the materials in Fig. 1(a) and (b) were identified as franklinite, $ZnFe_2O_4$.

Euhedral crystals up to several micrometers across were observed in samples A and B (Fig. 1(c) and (d)). EDX spectra from these crystals (Table 2) are similar to those from the fine-grained franklinite. Single-crystal diffraction patterns from the euhedral crystals are consistent with a cubic structure with the lattice parameter of franklinite (space group $Fd\overline{3}m$, $a = \sim 0.845$ nm; e.g., [7,8]). Some diffraction patterns show kinematically forbidden reflections such as {020} and {240} (with d-spacings of 0.422 and 0.189 nm, respectively).

Franklinite ($ZnFe_2O_4$, also known as zinc ferrite) is a member of a large, industrially and geologically important group of materials known as 'oxide spinels.' Oxide spinels have the general formula AB_2O_4, where A is typically a cation with a +2 charge such as Mg, Mn^{2+}, Fe^{2+}, Co, Ni, or Cu and B is typically a cation with a +3 charge such as Fe^{3+}, Mn^{3+}, Al, or Cr (e.g., [9,10]). End-member oxide spinel compositions involving cations likely to be present in crud include $ZnFe_2O_4$ (franklinite), Fe_3O_4 (magnetite), $MnFe_2O_4$ (jacobsite), $NiFe_2O_4$ (trevorite), $FeCr_2O_4$ (chromite), $MgCr_2O_4$ (magnesiochromite), $MnCr_2O_4$ (manganochromite), $NiCr_2O_4$ (nichromite), $ZnCr_2O_4$, $FeAl_2O_4$ (hercynite), $ZnAl_2O_4$ (gahnite), and $MgAl_2O_4$ (spinel). All of these minerals belong to space group $Fd\overline{3}m$. Substitutions into both A and B sites leading to intermediate compositions are common, and do not change the lattice parameters enough to be recognizable from selected-area electron diffraction patterns. In particular, up to ~10% MnO, 3% Al_2O_3, 1% MgO, and 1% TiO_2 have been reported in naturally occurring franklinite [7].

The EDX spectra from fine-grained franklinite (Table 1) show relatively low concentrations of numerous elements in addition to the Zn and Fe expected from stoichiometric franklinite. Some of these elements (particularly Cu, Mn, and Al) occur in end-member oxide spinels. Because of the similar structures and lattice parameters of many oxide spinels, it was not possible to determine whether these elements occur in the fine-grained materials in solid solution in the franklinite, in separate oxide spinels, or in small quantities of other phases not represented in the diffraction data.

4.2. Willemite (Zn_2SiO_4)

Table 3 shows EDX data from a single particle from sample B. The composition of this particle is consistent with either willemite, Zn_2SiO_4, or hemimorphite, $Zn_4Si_2O_7(OH)_2 \cdot H_2O$. The d-spacings

Table 2
EDX data from euhedral crystals of franklinite, samples A and B

Element	Spectrum A-2		Spectrum A-24		Spectrum A-25		Spectrum A-28		Spectrum A-29		Spectrum B-19	
	wt%	at.%	wt%	at.%	wt%	at.%	wt%	at.%	wt%	at.%	wt%	at.%
Na					2.7	6.6	6.1	14.2	3.9	9.3	3.9	9.4
Al			1.4	3.0	0.4	0.8	0.3	0.5	0.6	1.2	0.3	0.5
Si					0.2	0.4			0.4	0.8	0.2	0.4
K											0.0	0.1
Ca											0.1	0.1
Cr	0.1	0.2			0.3	0.3					0.0	0.0
Mn	3.2	3.4	7.2	7.7	9.9	10.1	8.8	8.6	2.2	2.2	0.4	0.4
Fe	60.3	63.7	48.1	50.4	47.2	47.6	46.9	45.2	56.7	56.0	61.5	60.7
Ni	0.3	0.3	0.7	0.7	2.2	2.1	3.1	2.8			1.0	0.9
Cu	0.2	0.2	1.1	1.0	0.7	0.6			0.4	0.3	0.0	0.0
Zn	35.6	32.1	37.2	33.3	36.5	31.5	34.9	28.7	35.9	30.3	32.6	27.5
Zr	0.2	0.2	1.1	0.7								

Locations from which spectra A-2, A-24, A-25, A-28, and A-29 were collected are shown in Fig. 1. Percentages of reported elements are normalized to a total of 100% for each spectrum.

Table 3
EDX data from willemite, sample B

Element	Spectrum B-24	
	wt%	at.%
Na	5.4	11.5
Al	0.9	1.6
Si	15.6	27.4
Cl	0.8	1.1
K	0.3	0.4
Ca	0.5	0.6
Fe	3.1	2.7
Co	1.2	1.0
Zn	70.7	53.2
Cs	0.4	0.1
U	1.1	0.2

Percentages of reported elements are normalized to a total of 100%.

and interplanar angles in eight single-crystal diffraction patterns collected from this particle are consistent with a hexagonal crystal with the lattice parameters of willemite (space group $R\bar{3}$, $a = 1.3928$ nm, $c = 0.9332$ nm, PDF4+ card 04-005-6483), although some show kinematically forbidden reflections. Although hemimorphite has proportions of Zn, Si, and O similar to those in willemite, the lattice parameters and space group (space group *Imm*2, $a = 0.8367$, $b = 1.0730$, $c = 0.5115$ [11]), are significantly different. Hemimorphite can be specifically ruled out as a possible identification for this particle because it could not have produced many of the experimental single-crystal diffraction patterns.

4.3. Iron oxides (including hydroxides and oxyhydroxides)

Hematite, akaganéite, and nanocrystalline mixed iron oxides were identified in the data presented here.

4.3.1. Hematite (α-Fe_2O_3)

Fig. 2 shows data from two particles from sample A whose EDX spectra (Table 4) indicate that they are iron oxides. Single-crystal diffraction patterns from these particles are consistent with a hexagonal crystal with the lattice parameters of hematite (space group $R\bar{3}c$, $a = 0.5038$ nm, $c = 1.3772$ nm [12]). The $(10\bar{1}1)$ and (0002) reflections identified in italics in Fig. 2(b) are kinematically forbidden, and are relatively weak. Although a few of the patterns from hematite in the PDF4+ database show weak reflections with d-spacings between 0.40 and 0.42 nm (corresponding to the $\{10\bar{1}1\}$ lattice planes), none show the 0.68–0.69 nm d-spacings corresponding to the $\{0002\}$ reflections shown in Fig. 2(b).

4.3.2. Akaganéite (β-FeOOH)

Diffraction patterns from several particles from sample B, whose EDX spectra suggest that they are Fe oxides with significant concentrations of Cl, show rings whose d-spacings correspond to high-intensity d-spacings of akaganéite (β-FeOOH). Akaganéite has a hollandite-type structure in which large channels are occupied by chloride ions, and (despite the nominal formula) contains structural

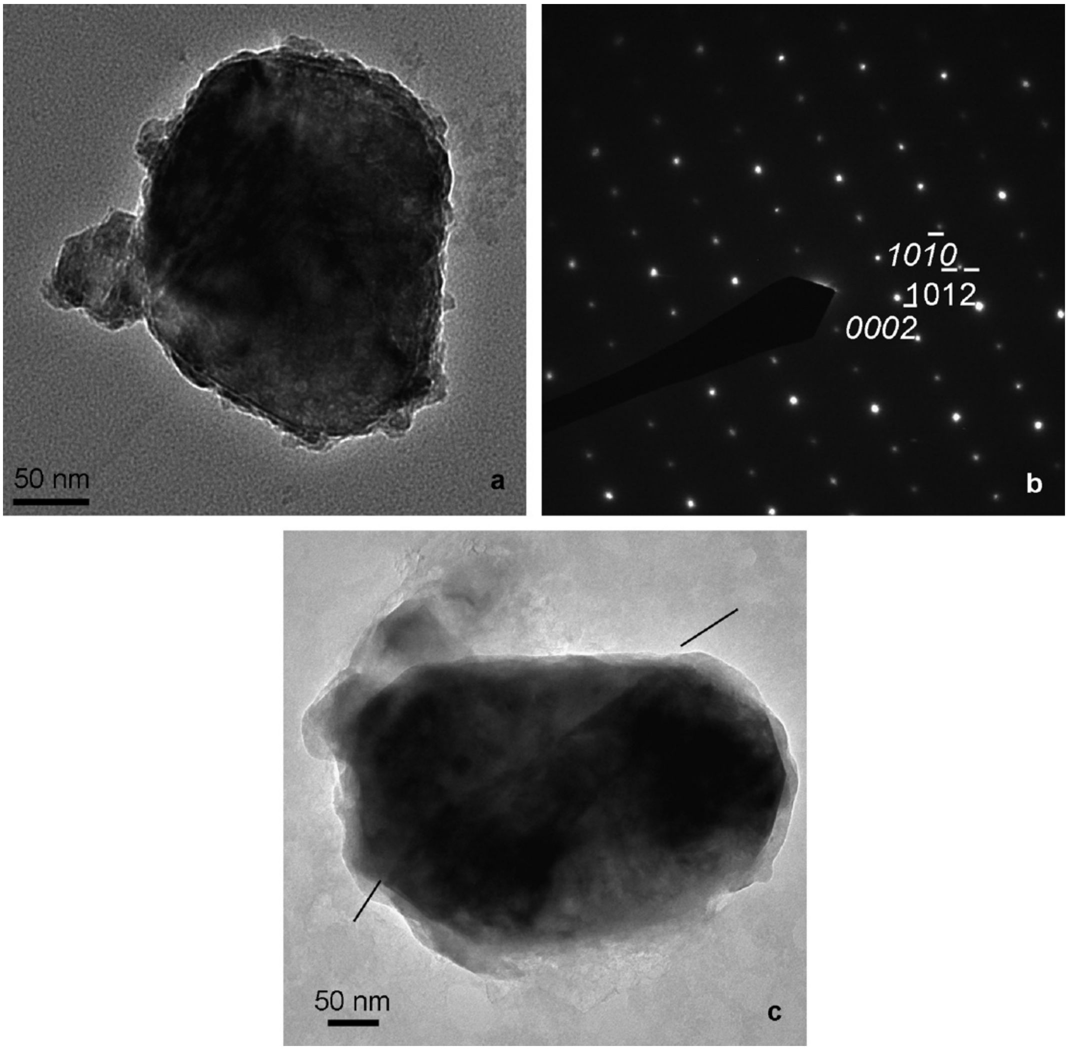

Fig. 2. Hematite (α-Fe_2O_3), sample A. (a) Image corresponding to EDX spectrum A-9 (Table 4). (b) $\langle 1\bar{2}10\rangle$ diffraction pattern from the crystal in part a showing faint kinematically forbidden reflections (examples identified in italic type). (c) Image of another particle. Lines near edges of crystal show ends of grain boundary. EDX spectrum A-15 (Table 4) is from the area to the right of the boundary.

Cl [13,14]. Some of the chloride can be removed by washing or dialysis; however, complete removal causes collapse of the structure and a phase transition to hematite (α-Fe_2O_3) or goethite (α-FeOOH) [15]. Because the akaganéite contains chloride (a contaminant), it probably formed after the fuel pins left the reactor.

4.3.3. Nanocrystalline Fe oxides

Fig. 3 shows an area of small crystallites from sample A. The corresponding EDX spectrum (Table 5) suggests that these crystallites are iron oxides. The d-spacings corresponding to rings in the diffraction pattern (Table 6) do not match high-intensity lines from any single iron oxide. Synthesizing pure iron oxides in the laboratory requires precise control of numerous conditions including solution and atmospheric compositions, pH, temperature, and oxygen fugacity, and some preparations must be washed immediately to prevent phase changes [15]. As these conditions were not controlled for the crud samples, mixtures are likely. Table 6 shows that a mixture of magnetite (Fe_3O_4), hematite (α-Fe_2O_3), and goethite (α-FeOOH) could match all of the d-spacings in Table 6, but might also produce rings corresponding to d-spacings not observed in the experimental data. d-spacings from lepidocrocite (γ-FeOOH) and akaganéite (β-FeOOH) are poor

Table 4
EDX data from hematite, sample A

Element	Spectrum A-9		Spectrum A-15	
	wt%	at.%	wt%	at.%
Na	0.32	0.78	1.55	3.68
Al	1.03	2.11	0.47	0.96
Si			0.87	1.68
Cl			0.35	0.54
K			0.19	0.27
Ca			0.53	0.73
Mn	0.42	0.42	0.97	0.96
Fe	96.53	95.49	91.47	89.30
Zn	0.74	0.63	0.63	0.53
Sr			0.82	0.51
Zr	0.96	0.58		
Ba			2.14	0.85

Spectrum A-9 is from the crystal shown in Fig. 2(a); spectrum A-15 is from the right section of the crystal shown in Fig. 2(b). Percentages of reported elements are normalized to 100% for each spectrum.

matches to the experimental data, and neither phase is likely to be present in significant quantities in this area of the sample. The lattice parameters and structure of cubic maghemite (γ-Fe_2O_3) are similar to those of magnetite, and distinguishing between these phases in nanocrystalline mixtures may be problematic. Thus, although the EDX and diffraction data clearly indicate a mixture of iron oxides not including akaganéite and lepidocrocite, the phases and proportions involved are unknown.

4.4. Silica

Fig. 4(a) (from sample A) is an image from a crystalline particle with numerous dislocations and a subgrain boundary. The corresponding diffraction pattern (Fig. 4(b)) was collected in an off-axis orientation to demonstrate that the particle is crystalline and was therefore not analyzed in detail. The EDX spectrum indicates that the particle is silica. This particle is probably quartz (α-SiO_2), the thermodynamically favored polymorph of silica at pressures and temperatures inside a reactor and in other earth-surface environments. Extensive experimental and geological evidence shows that quartz does not precipitate directly from dissolved silica in hydrothermal systems, but instead forms by transformation of amorphous silica (possibly through one or more intermediate crystal structures). Transformation mechanisms are complex and may depend on trace-element chemistry, and kinetics of quartz formation are poorly understood (e.g., [16]). Thus, it is possible that the crystalline silica was somehow introduced from outside the reactor (possibly as blowing quartz sand).

Fig. 4(c) (from sample B) shows an electron-transparent particle whose EDX spectrum indicates that it is silica. The diffraction pattern (Fig. 4(d)) has faint, diffuse, discontinuous rings. d-Spacings represented by the rings do not correspond to those expected from silicon monoxide (SiO) or any of the SiO_2 polymorphs likely at ambient temperatures (α-quartz, low cristobalite, low tridymite, coesite, and stishovite), but instead are those expected from halite (NaCl, which was commonly observed in this sample). Thus, it seems likely that this particle is amorphous SiO_2, and that the diffraction pattern is produced by small amounts of nanocrystalline halite (a contaminant) in the same particle.

4.5. Unidentified phases

A few crystals of a phase with 30–50% Ba and 10–20% S were observed in sample A. Diffraction patterns show highly discontinuous rings, indicating a strong crystallographic preferred orientation. Although d-spacings were measured from several of the patterns, it was not possible to match them to any high-Ba, high-S phase in the PDF4+ database.

One particle of a phase that has a Fe:Cr ratio of ~4:1 and significant concentrations of Ni and Si was found in sample B. Although most of the particle is not electron transparent, data were collected from a few thin areas at the edges of the particle. Radii of rings in diffraction patterns suggest that this phase has d-spacings of 0.095, 0.100, 0.112, 0.130, 0.169, 0.194, and 0.228 nm. These d-spacings do not match the high-intensity peaks for any Fe, Fe–Cr or Fe–Cr–Ni phase (with or without light elements and silicon) in the PDF4+ database. Images suggest that this phase may have a platy habit, and that individual electron-transparent crystallites consistently have their flat sides approximately parallel to the plane of the specimen. Thus, the observed d-spacings may reflect a strong crystallographic preferred orientation.

5. Discussion and conclusions

This paper reports identification of phases in crud from two operating boiling-water reactors used in commercial power generation. The phases were

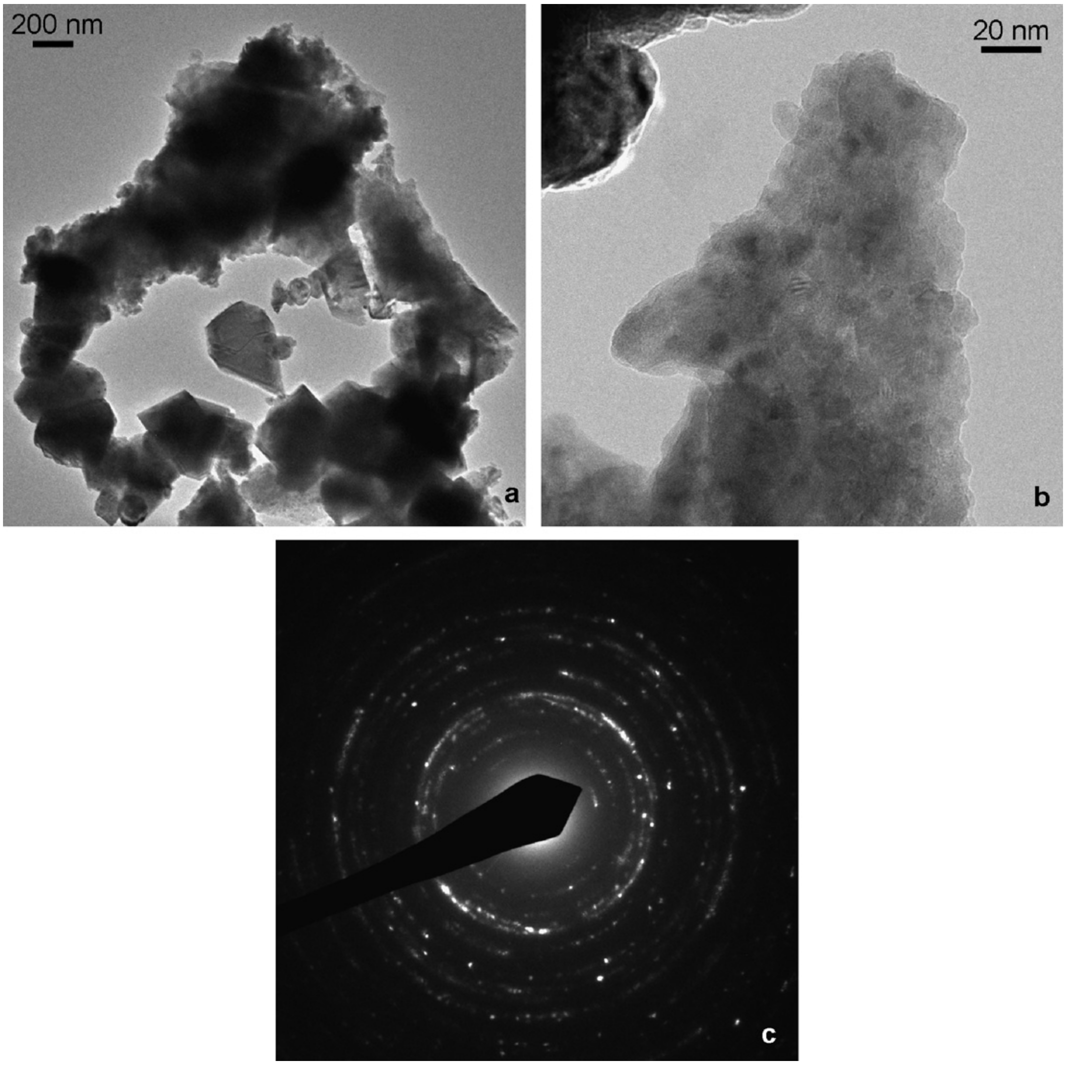

Fig. 3. Nanocrystalline iron oxides, sample A. (a) Low-magnification image providing overview of entire particle. Black arrow shows an area of nanocrystalline iron oxides. White arrows show areas whose EDX spectra indicate that they are franklinite. (b) Higher magnification image of area indicated by black arrow in part a showing crystallite sizes. (c) Diffraction pattern corresponding to (b).

identified by a combination of energy-dispersive X-ray spectroscopy (EDX) and selected-area electron diffraction in a transmission electron microscope. Samples were prepared by suspending minuscule particles in pure water, placing a drop of the water on a carbon-coated formvar substrate, and air drying. Relative abundances of phases in the TEM samples are probably not statistically representative, and it is likely that the bulk samples contain phases that were not observed in this study. Nonetheless, TEM offers a unique opportunity to identify the phases and observe the compositions of individual crystals. It is thus is a worthwhile complement to data produced by techniques such as scanning electron microscopy and chemical analysis of dissolved samples.

One surprising result is that both samples contained chloride-bearing phases (primarily NaCl, but also KCl and akaganéite). Some EDX spectra from SEM analyses of material collected from the same location at the same time as sample B conducted by an independent laboratory also showed chlorine [6]. As it is highly unlikely that significant concentrations of chlorine would be tolerated in a reactor cooling system, the chloride-bearing phases are apparently contaminants that were somehow introduced between the time the fuel pin was removed from the reactor and the time the samples

Table 5
EDX data from nanocrystalline iron oxides, sample A

Element	Spectrum A-31	
	wt%	at.%
Na	4.44	10.49
Al	1.76	3.55
Si	0.71	1.38
K	0.54	0.75
Ca	0.76	1.03
Cr	1.54	1.61
Mn	1.26	1.25
Fe	69.80	67.95
Zn	6.06	5.04
Zr	8.74	5.21
Ba	4.40	1.74

Data is from the area shown in Fig. 3, and corresponds to the d-spacings in Table 6. Percentages of reported elements are normalized to 100%.

Table 6
d-Spacings (in nm) from rings from nanocrystalline iron oxides and PDF4+ data showing all d-spacings with intensities ⩾10% of the highest intensity peak for each spectrum from three iron oxides that may contribute to the diffraction pattern (Fig. 3(c))

Fig. 3(c)	Hematite (PDF4+ card 04-008-8479)	Magnetite (PDF4+ card 04-005-4307)	Goethite (PDF4+ card 01s-081-0464)
0.497			0.498
		0.485	
			0.418
0.366	0.369		
			0.338
0.306			
		0.297	
0.272	0.270		0.269
0.255	0.252	0.253	0.258
0.247			0.245 + 0.249
0.224	0.221		0.219 + 0.225
0.209		0.210	
0.185	0.184		
0.173	0.170		0.172
0.162		0.162	

were sent to be analyzed. The common presence of chloride-containing contaminant phases is obvious, and suggests that other contaminant phases whose compositions are more compatible with cooling-water chemistry (e.g., the crystalline silica from sample A) may also be present. If quantities of contaminants in the samples studied here are typical, the inclusion of unrecognized contaminant phases in SEM and chemical analysis data from other samples may greatly complicate attempts to understand and prevent the formation of crud.

Franklinite ($ZnFe_2O_4$) and halite (a contaminant) were the only phases observed in both samples. Other phases observed in sample A included hematite (α-Fe_2O_3), crystalline silica (SiO_2), a fine-grained mixture of iron oxides probably including magnetite (Fe_3O_4), hematite (α-Fe_2O_3), and goethite (α-FeOOH), and an unidentified high-Ba, high-S phase. Other phases observed in sample B included sylvite (KCl), akaganéite (β-FeOOH), willemite (Zn_2SiO_4) and amorphous silica, and an unidentified Fe–Cr phase. Halite was relatively uncommon in data from sample A and ubiquitous in observations from sample B. Because of the small sample volumes and numbers of particles studied and the possibility that some of the phases were introduced as contaminants outside the reactor, it is not clear whether the differences between the phases observed in the two crud samples are characteristics of the samples or artifacts of the lack of statistical representation in the data.

Some single-crystal electron-diffraction patterns from franklinite show kinematically forbidden reflections. Forbidden {200} reflections in X-ray powder patterns from franklinite were determined to be from double diffraction [7]. Careful studies of kinematically forbidden reflections in electron diffraction patterns from spinel ($MgAl_2O_4$), which has the same structure as franklinite, indicated that these reflections were also produced by double diffraction [17]. Polycrystalline diffraction patterns from the fine-grained franklinite do not show d-spacings corresponding to the forbidden reflections. All of these observations suggest that the kinematically forbidden reflections from the franklinite in the crud are from double diffraction rather than from differences between the franklinite observed here and that forming in geological environments.

Kinematically forbidden reflections were also observed in some diffraction patterns from hematite and willemite. Detailed analyses of the factors allowing the appearance of kinematically forbidden reflections can be quite complex (e.g., [18,19]), and are beyond the scope of this paper. Although the origins of the kinematically forbidden reflections in willemite and hematite are unknown, these reflections are not considered sufficient reason to discard these identifications.

TEM–EDX analyses commonly show the presence of elements not expected from phase identifications based on diffraction data, particularly in nanocrystalline areas, and some diffraction patterns

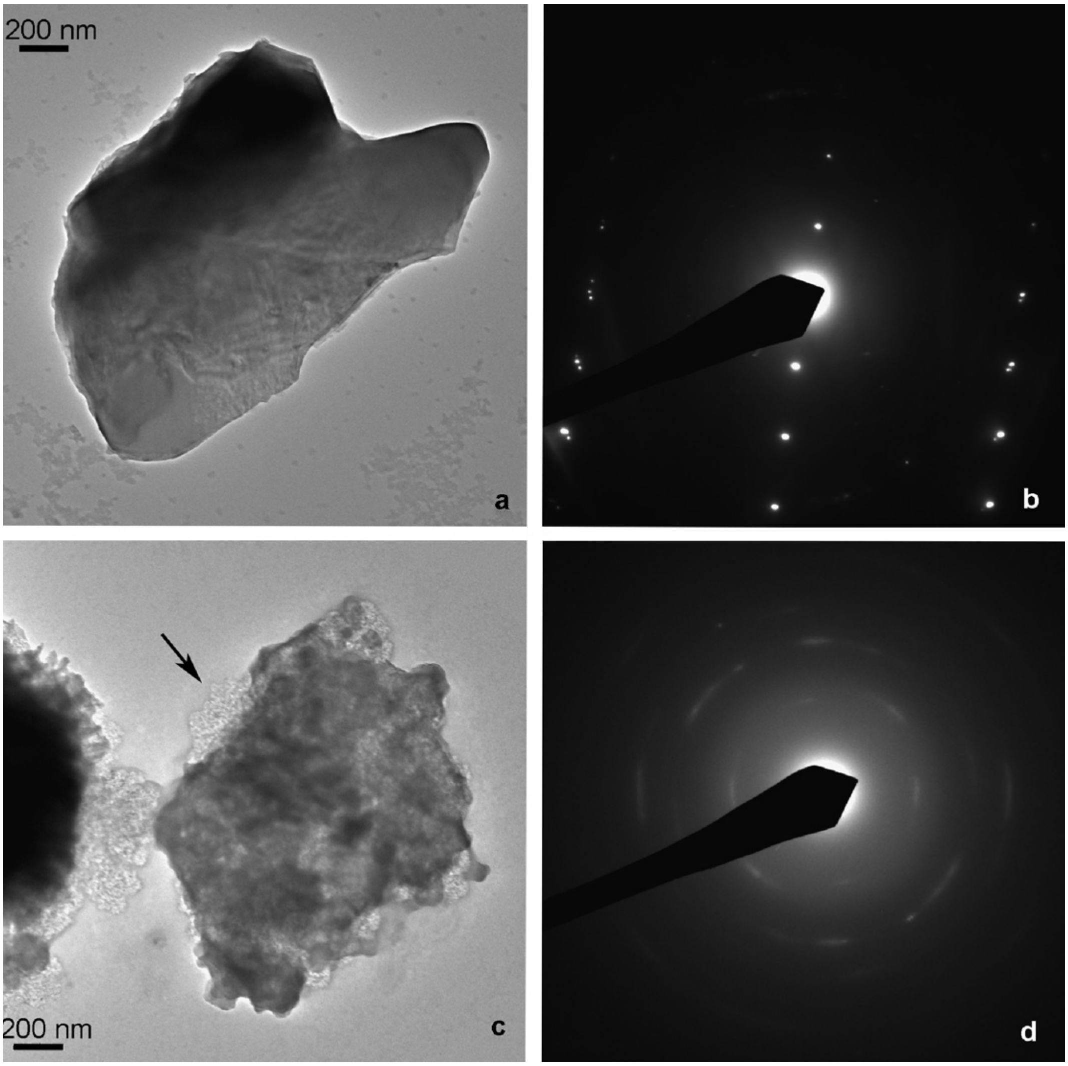

Fig. 4. Silica, samples A and B. (a) Image showing particle of crystalline silica from sample A. (b) Off-axis diffraction pattern from particle in part a. Pairs of closely spaced reflections are probably from different sub-grains. (c) Particle of amorphous silica from sample B. Note the light-colored material around the edges of the particle (e.g., at arrow), which may be halite (a contaminant). The large particle at the left of the image is akaganéite. (d) Diffraction pattern from this particle showing four faint, diffuse, highly discontinuous rings whose d-spacings correspond to those of halite.

with rings also show reflections apparently produced by single crystals of phases not represented by the rings. Although some of the 'extra' elements may be present in solid solutions, it is likely that many of the EDX analyses include X-rays from small quantities of phases that were not identified from the diffraction data.

All of the available data indicate that crud consists of a complex, multi-phase assemblage with spatial variation that can only be understood in detail using techniques with high spatial resolution such as TEM. However, these techniques survey areas too small to identify broader patterns of compositional variation throughout the entire thickness of a crud layer, such as can be observed with SEM. Bulk chemical analyses provide relatively easy ways to observe gross changes in crud characteristics as a result of changes in water chemistry or reactor operation, but are of limited use in identification of individual phases in complex assemblages. Identification of individual phases in X-ray diffraction patterns from complex assemblages can be prohibitively difficult. Thus, crud is probably best understood by a variety of analytical techniques, each of which has its own strengths and weaknesses. TEM is clearly one such technique.

Acknowledgments

The authors would like to thank Dr Bo Cheng, the EPRI Project Manager for this study. We would also like to thank Dr Kurt Edsinger (EPRI), who arranged for the samples described in this publication to be provided to the Idaho National Laboratory (INL). Dr Cheng, Dr George Sabol, and Dr Mike Pop provided helpful comments on preliminary presentations of this work. Mr Dan Lutz (General Electric) was instrumental in helping us to obtain the samples analyzed here. Comments by an anonymous reviewer are also appreciated.

The work was performed in the Electron Microscopy Laboratory at the INL, and the authors would like to thank EML staff members Dr Tom O'Holleran and Mr Mark Surchik for their assistance. Mr Calvin D. Morgan (from the Analytical Laboratory at the INL) analyzed the chloride content of the water used for sample preparation. Ms. Mary Schlegel (INL) provided expert assistance in typing and formatting a more comprehensive report that was the source of the information provided here, and Mr Keener Earle provided project-management services at the INL.

The work was supported by the US Department of Energy, Office of Nuclear Energy, Science, and Technology, under DOE Idaho Operations Office Contract DE-AC07-05ID14517. The authors would particularly like to thank our sponsor, Tom Miller from DOE NE-30, who graciously funded this work.

References

[1] S. Uchida, Y. Asakura, K. Ohsumi, M. Miki, M. Aizawa, Y. Matsushima, K. Yonezawa, J. Nucl. Sci. Technol. 24 (1987) 385.
[2] C.S. Olsen, Nucl. Eng. Des. 89 (1985) 51.
[3] Y. Nishino, T. Sawa, K. Ebara, H. Itoh, J. Nucl. Sci. Technol. 26 (1989) 249.
[4] T. Mizuno, K. Wada, T. Iwahori, Corrosion–NACE 38 (1982) 15.
[5] K. Ishigure, Radiat. Phys. Chem. 22 (1983) 119.
[6] G. Sabol, Report 1011748, Electric Power Research Institute, Palo Alto, CA, 2005.
[7] S. Lucchesi, U. Russo, A. Della Giusta, Eur. J. Mineral. 11 (1999) 501.
[8] H.S.C. O'Neill, Eur. J. Mineral. 4 (1992) 571.
[9] R.J. Hill, J.R. Craig, G.V. Gibbs, Phys. Chem. Miner. 4 (1979) 317.
[10] G.A. Waychunas, Crystal Chemistry of Oxides and Oxyhydroxides, in: D.H. Lindsley (Ed.), Oxide Minerals: Petrologic and Magnetic Significance, Mineralogical Society of America, Washington, DC, 1992, p. 11.
[11] R.J. Hill, G.V. Gibbs, J.R. Craig, F.K. Ross, J.M. Williams, Z. Kristallogr. 146 (1977) 241.
[12] R.L. Blake, R.E. Hessevick, T. Zoltai, L.W. Finger, Am. Mineral. 51 (1966) 123.
[13] J.E. Post, V.F. Buchwald, Am. Mineral. 76 (1991) 272.
[14] J.E. Post, P.E. Heaney, R.B. Von Dreele, J.C. Hanson, Am. Mineral. 88 (2003) 782.
[15] U. Schwertmann, R.M. Cornell, Iron Oxides in the Laboratory: Preparation and Characterization, 2nd Ed., Wiley-VCH, Weinheim, Germany, 2000.
[16] P. Bettermann, F. Liebau, Contrib. Mineral. Petrol. 53 (1975) 25.
[17] M. Tokonami, H. Horiuchi, Acta Crystallogr., A 36 (1980) 122.
[18] P. Hirsch, A. Howie, R. Nicholson, D.W. Pashley, M.J. Whelan, Electron Microscopy of Thin Crystals, Krieger Publishing Company, Malabar, FL, 1977.
[19] D.B. Williams, C.B. CarterTransmission Electron Microscopy Diffraction, vol. 2, Plenum, New York, 1996.